Epitaxial Photostriction–Magnetostriction Coupled Self-Assembled Nanostructures

Heng-Jui Liu,[†,Δ] Long-Yi Chen,[‡,Δ] Qing He,[§] Chen-Wei Liang,[#] Yu-Ze Chen,[†] Yung-Shun Chien,[⊥] Ying-Hui Hsieh,[#] Su-Jien Lin,[†] Elke Arenholz,[§] Chih-Wei Luo,[‡] Yu-Lun Chueh,[†] Yi-Chun Chen,[⊥] and Ying-Hao Chu[#,*]

[†]Department of Materials Science and Engineering, National Tsing Hua University, Hsinchu 30013, Taiwan, [‡]Department of Electrophysics, National Chiao Tung University, Hsinchu 30010, Taiwan, [§]Advanced Light Source, Lawrence Berkeley National Laboratory, Berkeley, California 94720, United States , [#]Department of Materials Science and Engineering, National Chiao Tung University, Hsinchu 30010, Taiwan, and [⊥]Department of Physics, National Cheng Kung University, Tainan 70101, Taiwan. [Δ]These authors contributed equally.

ABSTRACT

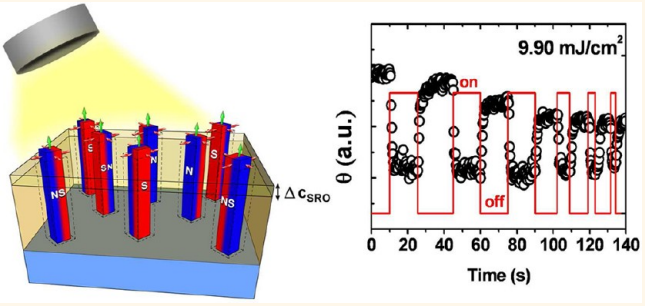

Self-assembled vertical nanostructures take advantage of high interface-to-volume ratio and can be used to design new functionalities by the choice of a proper combination of constituents. However, most of the studies to date have emphasized the functional controllability of the nanostructures using external electric or magnetic fields. In this study, to introduce *light* (or *photons*) as an external control parameter in a self-assembled nanostructure system, we have successfully synthesized oxide nanostructures with $CoFe_2O_4$ nanopillars embedded in a $SrRuO_3$ matrix. The combination of photostrictive $SrRuO_3$ and magnetostrictive $CoFe_2O_4$ in the intimately assembled nanostructures leads to a light-induced, ultrafast change in magnetization of the $CoFe_2O_4$ nanopillars. Our work demonstrates a novel concept on oxide nanostructure design and opens an alternative pathway for the explorations of diverse functionalities in heteroepitaxial self-assembled oxide nanostructures.

KEYWORDS: self-assembled · nanostructures · photostrictive $SrRuO_3$ · magnetostrictive $CoFe_2O_4$ · pump–probe technique · MFM · coupling

The interplay of lattice, charge, orbital, and spin degrees of freedom in complex oxides covers a broad spectrum of intriguing functionalities and offers tremendous opportunities for next-generation electronic devices.[1,2] Over the past decade, advanced synthesis techniques assisted with *in situ* characterizations have been applied to demonstrate complex oxide thin films and various combinations of heterostructures, suggesting new possibilities to create and design devices with tantalizing functionalities.[3,4] Among them, one type of heterostructure drawing a considerable spotlight is high interface-to-volume ratio vertical nanostructures.[5,6] Vertical nanostructures can be used to impose heteroepitaxial strain on a material to tune the properties thereof. Examples can be found in the (La,Ca)MnO_3–MgO system with tunable Curie temperatures[7] or the $BaTiO_3$–$CoFe_2O_4$ (CFO) system with enhanced interfacial coupling.[8] Several studies have also proposed the various tunability of nanostructures through substrate engineering, such as the inverse ability of the nanostructures,[9,10] the tunable ferroelectric polarization of the matrix,[11] and the misorientation of the nanopillars and matrix.[12] These studies successfully demonstrated more possible combinations to tailor the properties of oxide nanostructures. In addition, new functionalities have been unveiled by the choice of a proper combination of constituents, for instance, magnetic-field-assisted electrically controllable magnetoelectric coupling in $BiFeO_3$–CFO,[13,14] low magnetic-field driven colossal magnetoresistance in (La,Sr)MnO_3–ZnO,[15] abnormal dielectric response in $BiFeO_3$–Sm_2O_3,[16] and enhanced ferroelectricity in $BaTiO_3$–Sm_2O_3.[17]

However, while most of the studies to date have stressed the functional controllability of heterostructures using external electric or magnetic fields, rarely has the attention been placed on exploring other external control parameters. Recently, a large photon-induced strain of ~0.5% to 1.5% was demonstrated in SRO/$SrTiO_3$[18] and SRO/Pb(Zr,Ti)O_3 superlattices.[19] Motivated by this, in order to introduce *light* (or *photons*) as an external control parameter in a

* Address correspondence to yhc@nctu.edu.tw.

Received for review May 4, 2012 and accepted June 30, 2012.

Published online July 01, 2012
10.1021/nn301976p

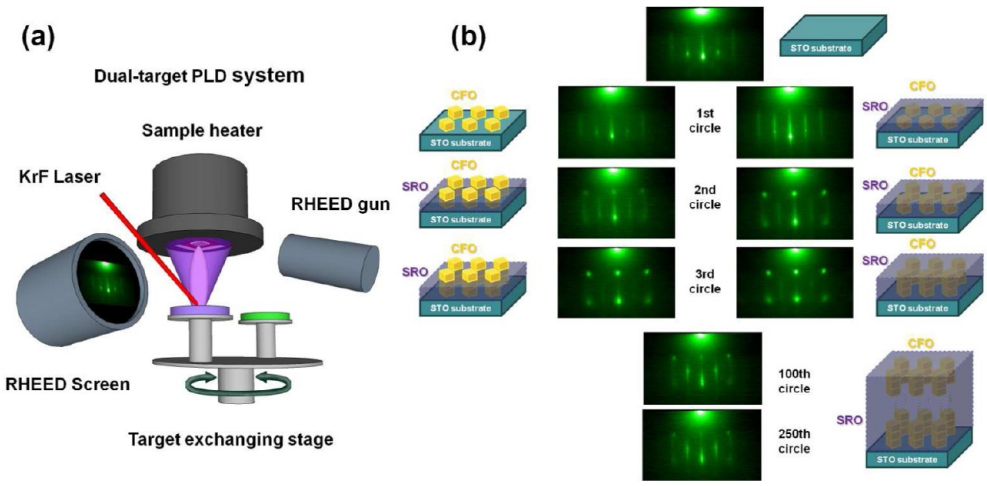

Figure 1. (a) Illustrations of the RHEED-assisted PLD setup. (b) RHEED patterns recorded during the CFO−SRO deposition. Patterns in the same row were recorded in the same alternation cycle. Right: Cartoons of the corresponding RHEED patterns are used to show the growth of the CFO−SRO nanostructures.

self-assembled nanostructure system, we chose a large photostrictive $SrRuO_3$ (SRO) as the matrix material to couple with the large magetostrictive CFO nanopillars. High-quality SRO−CFO nanostructures were successfully synthesized and evidenced by X-ray diffraction and transmission electron microscopy. Ultrafast dynamics based on the pump−probe technique was used to probe the photostriction of the SRO matrix. Macroscopic magnetic measurement and X-ray magnetic circular dichorism were applied to confirm the magnetic contribution from the CFO nanopillars at room temperature. The coupling between the photostricitive SRO matrix and the magnetostrictive CFO nanopillars was evidenced by the magneto-optic Kerr effect and magnetic force microscopy (MFM). Through the lattice coupling between SRO and CFO, the nanostructured composite thin film shows more interesting features, which can potentially be used to improve thermal stability due to a high uniaxial magnetic anisotropy, light-assisted low magnetic field switching, and self-bit patterned magnetic media with a recording density of 1Tbit/in.^{2} or more.[20−22] Our study paves the way to ultrafast optical-coupled functionalities in vertical heteroepitaxial nanostructures and develops a new type of magneto-optical materials.

RESULTS AND DISCUSSION

Pulsed laser deposition was used in this study for the preparation of CFO−SRO nanostructures (on $SrTiO_3$ (STO) (001) substrates). Different from the earlier works on oxide nanostructures, which mostly used a single target with all constituent elements mixed, a dual-target technique[23] was employed to synthesize CFO−SRO nanostructured thin films. As shown in Figure 1a, two ceramic discs (one CFO and one SRO) were used as the targets that fed the substrates separately. These two targets were mounted on an exchanging stage automated by an external motor and were shot by laser pulses alternatively during the deposition. The end product of the deposition was a SRO−CFO composite thin film with their ratio of around 0.35−0.4 controlled by the number of laser pulses received by each target. The dual-target deposition gives the flexibility to manipulate the composition of oxide thin films by the pulse number, which is not achievable in single-target deposition. To avoid the formation of multilayered structures, the number of laser pulses shot on the CFO and SRO targets was further controlled so that neither of the two materials grew more than one unit cell in thickness in each alternation cycle.

Figure 1b shows the reflection high-energy electron diffraction (RHEED) patterns recorded by a CCD camera during the thin-film growth. The array of straight lines resulting from the surface electron diffraction indicates the flat surface of the blank STO substrate. In the first alternation cycle, the intensity of the specular spot lines decreased once CFO was deposited, indicating the STO surface was roughened by CFO islands. Interestingly, the successive SRO deposition resulted in an intensity increase of the specular spot lines, showing the growth of SRO smooths the surface by filling the surrounding area of the CFO islands. The RHEED patterns of the consecutive cycles of the CFO−SRO deposition (the second and third cycles) show a spot-like feature with increasing intensities that is similar to the expected CFO pattern.[12] This implies that the CFO pillars start to evolve from the SRO surface at a very early stage (since the second cycle), and the smoothing resulting from SRO becomes less effective. Upon further increasing the deposition cycles, the RHEED pattern reveals more diffraction spots of CFO, which are contributed from the bulk diffraction due to the gradually growing islands on the surface. These mature islands also increase the probability of electron scattering and hence weaken the intensity of the diffraction

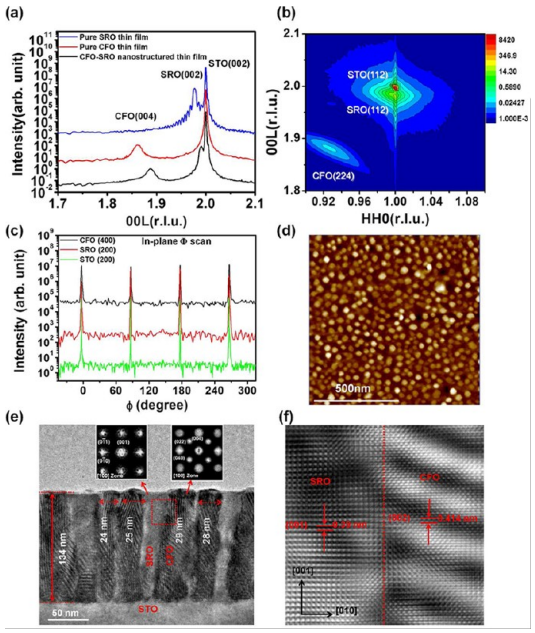

Figure 2. (a) XRD $2\theta-\theta$ scans around the STO(002) peak of the CFO−SRO nanostructures, pure CFO thin film, and pure SRO thin films. (b) Off-normal RSM scan around the STO-(112) peak. The SRO(112) and CFO(224) can be observed. (c) In-plane epitaxy revealed by Φ scans of CFO (400), SRO (200), and STO (200) peaks. (d) Topology (AFM) of the CFO−SRO nanostructures. (e) Cross-sectional TEM image of CFO−SRO nanostructures. CFO nanopillars are clearly shown with a darker contrast. Electron diffraction patterns from SRO and CFO are shown in the left and right insets, respectively, on top of the image. (f) TEM images of the CFO/SRO interface, marked in the red area in (e), with atomic resolution.

pattern. It is noticed that with the evolving spot feature, the streaks still survive on the diffraction patterns even for more than 250 deposition cycles, suggesting that the remaining region is flat.

The thin-film structure and epitaxy were studied using X-ray diffraction techniques. The $\theta-2\theta$ scan (Figure 2a) of the CFO−SRO thin film shows that both CFO and SRO are grown epitaxially on the STO (001) substrates, and only STO(002), SRO(002), and CFO(004) are observed in the scan. The *c*-axis lattice constants of the SRO and CFO are found at 3.9305 and 8.29 Å, respectively. To realize the strain correlation between SRO and CFO, we compare the *c*-axis lattice constants of CFO and SRO in the nanostructured thin film to those of pure CFO and pure SRO thin films with the same thickness on STO. The *c*-axis constant of pure CFO thin films is very close to the bulk value (c = 8.39 Å), which means that pure CFO grown on the STO substrate almost relaxes. On the other hand, the pure SRO thin film shows a larger *c*-lattice parameter (c = 3.952 Å) with a flat surface feature (thickness fringes), indicating that SRO is well strained on STO. However, in the nanostructured thin film, the CFO nanopillars suffer a vertical compressive strain (~1.1%) constrained by the relaxed SRO lattice instead of STO substrate. Further structural information is extracted by reciprocal space mapping (RSM, Figure 2b) around the STO (112) diffraction peak. According to the map, the in-plane (IP) lattice parameters of SRO and CFO are identified as 3.927 and 8.45 Å. Therefore, the *c*/*a* ratios for SRO and CFO are 1.0008 and 0.981, respectively. Compared to the bulk CFO lattice parameters ($a = b = c$ = 8.39 Å), our results show that CFO in the CFO−SRO thin film is subjected to out-of-plane (OOP) compressive strain. Calculation based on SRO (001) and CFO (002) lattice parameters yields a mismatch around 5.6% along [001], and this huge mismatch is expected to be accommodated by the formation of semicoherent interfaces.[24] In addition, 4-fold symmetry is also observed in STO, SRO, and CFO in the Φ-scan measurements, showing that the SRO−CFO thin films grew on the STO (001) substrate in a cube-on-cube fashion (Figure 2c). The morphology of the resultant thin films was studied by atomic force microscopy (AFM). Nanoscale square-shaped dots dispersed in a flat matrix are observed in the AFM measurement, as shown in Figure 2d. The size of each nanodot is around 50 nm or less. The spacing between these dots varies from 10 to 100 nm, resulting in an average density of ~120 dot/μm^2.

Furthermore, transmission electron microscopy (TEM) was used to investigate the microstructure and confirm the epitaxial relationship between CFO and SRO. The low-magnification TEM image shown in Figure 2e reveals that the CFO dots observed by AFM are actually nanopillars embedded in a continuous SRO matrix. Insets in Figure 2e are the corresponding diffraction patterns extracted by fast Fourier transform, confirming that pillars are CFO and the matrix is SRO. In addition, the epitaxial relationships of (001) CFO//(001) and [100] CFO//[100] SRO for CFO nanopillars and the SRO matrix are found. The high-resolution TEM image was taken from the marked region shown in Figure 2f. The TEM data are consistent with XRD results, suggesting a high-quality epitaxial self-assembled nanostructure.

In order to show the functionalities, such as electrical conduction and photostriction in SRO and electrical insulation and ferrimagnetism in CFO, conductive AFM (C-AFM), magnetic, and photostriction measurements were carried out. Figure 3a shows the AFM image as well as its corresponding C-AFM image (dc voltage: 1 V). The conduction in the matrix is much larger than that in the nanopillars, showing the insulating nature of CFO and the conducting behavior of SRO. The magnetism of the CFO−SRO nanostructures was studied using superconducting quantum interference device (SQUID) magnetometry measurements. Clear hysteresis of magnetization was observed when scanning the magnetic field back and forth between 70 and −70 kOe in the OOP direction at 300 K. Assuming that the magnetism is mainly contributed from CFO nanopillars, the calculated OOP magnetization saturates around ±350 emu/cm^3, which is close to the CFO bulk value, and the coercive field is around ±9000 Oe

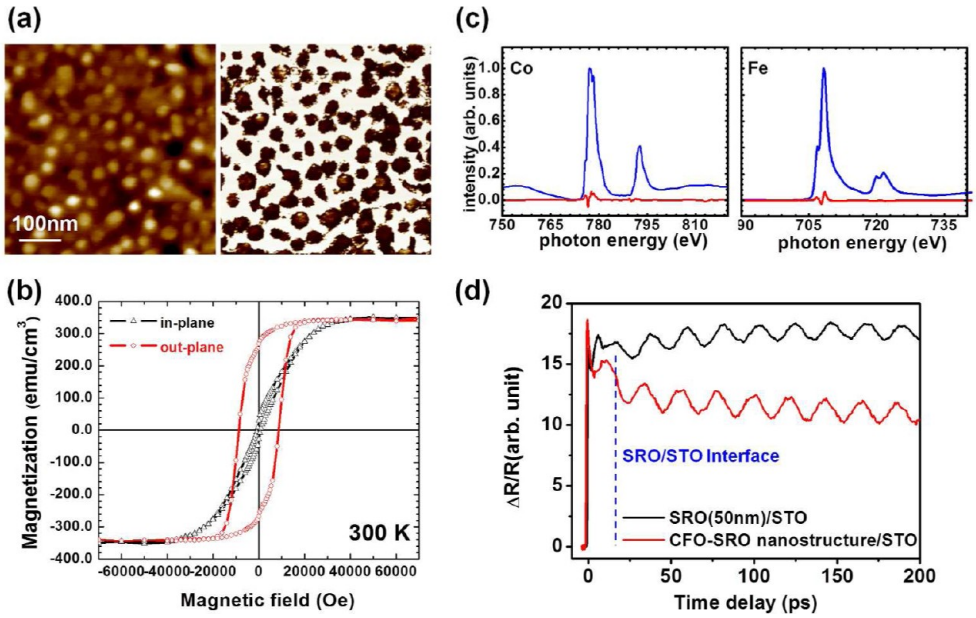

Figure 3. (a) AFM topology (left) and C-AFM image (right) of the CFO-SRO nanostructures. Both images are recorded at the same area. (b) SQUID measurements on the CFO−SRO nanostructures along the OOP and IP directions. (c) Results of the polarization-averaged soft XAS (blue) as well as the corresponding XMCD (red) obtained from the L-edges of Co (left) and Fe (right). (d) Results of the ultrafast $\Delta R/R$ measurements on CFO−SRO nanostructures and pure SRO thin films. Oscillations have been observed in both types of samples. The dashed line indicates the moment when the acoustic wave of SRO, excited by the laser pulse, hits the SRO/STO interface.

(Figure 3b). However, measurements of the IP magnetization did not show a well-defined ferromagnetic hysteresis loop, implying a hard axis for the IP magnetization of the CFO nanopillars. (The magnetic contribution from the SRO matrix is not expected since SRO becomes ferromagnetic only at temperatures below 150 K.) The magnetic data together with XRD and TEM data suggest the magnetic anisotropy is present due to the magnetostriciton in CFO.[25] In addition, X-ray magnetic circular dichroism (XMCD) was also performed. Soft X-ray absorption spectra (XAS) from CFO−SRO nanostructures in total electron yield configuration with a beam area of ~0.01 mm^2 at room temperature were taken at Advanced Light Source, Lawrence Berkeley National Laboratory, Beamline 4.02. We observed a clear signal at Fe and Co (Figure 3c) L-edges and Ru M-edge (not shown here). Based on Figure 3c, the valence states and the occupation sites of Fe and Co are analyzed and consistent with the CFO crystal, suggesting the spinel phase is CFO chemically. The difference in the absorption spectra using right and left circularly polarized light is a measure of ferromagnetism in the material. The presence of XMCD is observed only from Fe and Co spectra (Figure 3c), recognizing CFO as the source of the ferromagnetic response in this system at room temperature. The XMCD magnetic loops show the same coercivity with SQUID measurements.

The photostrictive effect of the SRO matrix was studied by the pump−probe measurements, where the sample was first illuminated by a Ti:sapphire laser operated at a repetition rate of 5.2 MHz and then the photoinduced transient reflectively changes ($\Delta R/R$) against the time delay were measured. The wavelengths of the pump and the probe beam were set at 400 and 800 nm, respectively. As shown in Figure 3d, similar oscillations in $\Delta R/R$ are observed in both CFO−SRO nanostrucutres and the pure SRO thin film (control experiment). For SRO, the pump pulse induces an electronic excitation that generates a mechanical stress of the lattice *via* the coupling of the electronic system to lattice degrees of freedom. The strain pulses generated on the surface of the SRO thin film propagate into the bulk and cause an oscillation in $\Delta R/R$ through the interference between the probe beams reflected by the thin film surface and the wavefront of the propagating strain pulse.[26] When strain pulses propagate through the SRO/STO interface, both the amplitude and period of the $\Delta R/R$ oscillation decrease. A discontinuity is clearly observed in the oscillation feature of $\Delta R/R$ after subtracting the decay background. A close look at the $\Delta R/R$ signal around zero time delay reveals that the oscillation signal starts within 5 ps. This indicates that the time needed to trigger strain pulses in SRO is less than 5 ps, suggesting a possibility to use this nanostructure in ultrafast applications. This set of experimental data confirms the photostrictive characteristics of SRO inside the nanostructures.

Direct evidence of impacts of light illumination on magnetic properties on this kind of nanostructure was then unambiguously revealed by magneto-optic Kerr effect (MOKE) measurements with the 632.8 nm light.

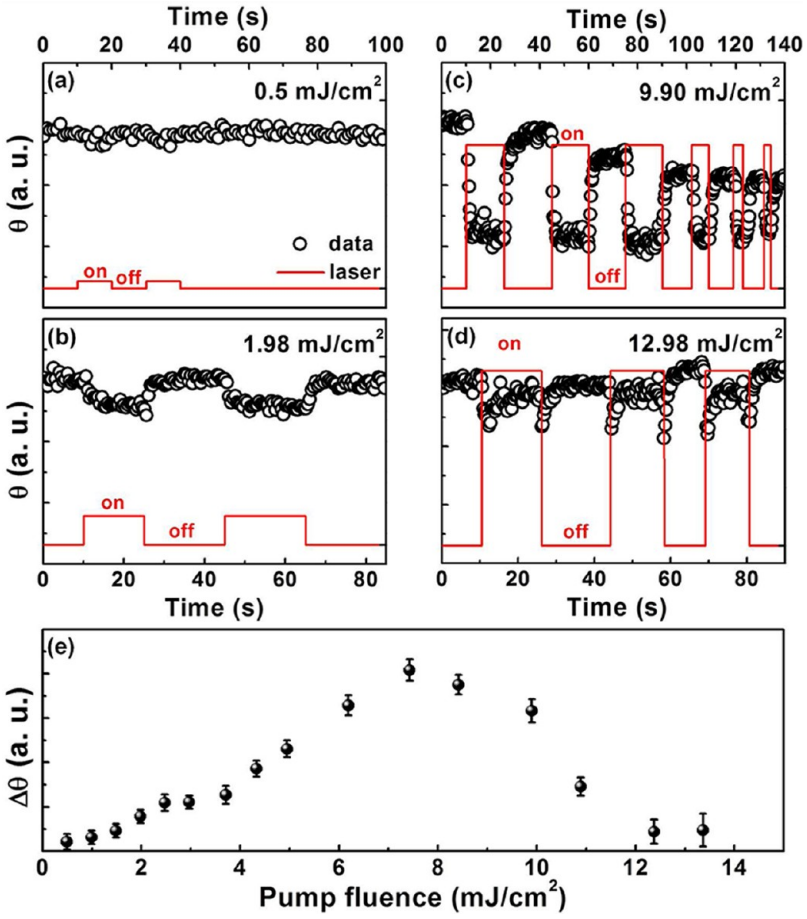

Figure 4. Kerr angle modulated by pump laser on/off in a CFO/SRO sample with fluences of (a) 0.5, (b) 1.98, (c) 9.90, and (d) 12.98 mJ/cm^2. (e) The pump fluence dependence of the Kerr angle changes between the first on and the first off of the pump laser. The MOKE measurements for probing the optical-modulation magnetic moment in CFO/SRO samples were carried out by using a HeNe laser (λ = 632.8 nm) and simultaneously pumped by a regenerative amplifier (repetition rate of 5 kHz and wavelength of 800 nm).

The sample was prepoled in the out-of-plane direction by a large magnetic field (7 T). Figure 4a–d show the typical evolution of the Kerr angle (θ, which is related to the total amount of out-of-plane magnetic moments) with and without the pumping of 800 nm light at various fluences. When the pump light illuminates the samples, the θ significantly decreases due to the tilts of magnetic moments with the release of vertically compressive strain in the CFO nanopillars, which is caused by the photostriction in the SRO matrix. Interestingly, the θ signal returns to the initial value after removing the 800 nm light. This implies that the magnetic moments in CFO nanopillars go back to the original out-of-plane direction prior to the laser pumping. In addition, this Kerr angle, *i.e.*, the effective amount of out-of-plane magnetic moments, can be modulated repetitively with the pump laser on and off; meanwhile, the modulation depth ($\Delta\theta$, Kerr angle variation) is strongly fluence-dependent, as shown in Figure 4e. The $\Delta\theta$ gradually increases while the fluence increases and then reaches a maximum at the pumping fluence of 7.5 mJ/cm^2. However, the $\Delta\theta$ will anomalously shrink when the pumping fluence is above the threshold of 7.5 mJ/cm^2. This suggests that the magnetic moment in CFO nanopillars returns to the original state below this threshold fluence and then becomes irreversible beyond that.

In order to understand the coupling mechanism and the irreversible behaviors, *ex situ* magnetic force microscopy measurements were applied. Samples of the CFO–SRO nanostructures were first magnetized with an OOP magnetic field (up to 7 T) and then illuminated by femtosecond pulses of a Ti:sapphire laser with a wavelength of 800 nm. The fluence is larger than the threshold value with a single pulse duration of 70 fs and a scan velocity of about 15 μm/s. After the femtosecond illumination, samples were submitted to MFM characterization. Results of the MFM measurements are shown in Figure 5, where the morphology (Figure 5a) and the MFM images before (Figure 5b) and after (Figure 5c) the illumination were obtained from the same area. The dark and bright contrasts shown in the MFM images represent the upward and downward magnetic polarizations, respectively. A large portion (~78.8%) of the before-illumination MFM image shows bright contrast, indicating that the CFO nanopillars are

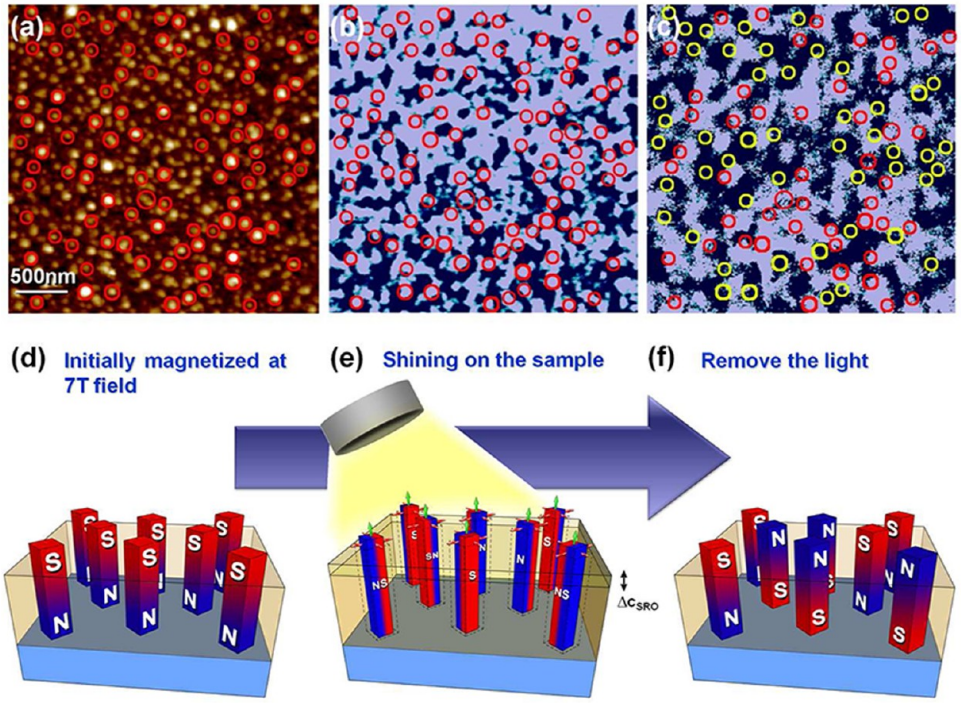

Figure 5. (a) AFM topology and (b) MFM image at the same area of a nanostructured CFO−SRO sample that has been magnetized by applying a large out-of-plane magnetic field before being illuminated. (c) MFM image at the same area after being illuminated. We randomly selected 100 nanopillars to conveniently observe the change in magnetic direction. The red circles in (b) are the nanopillars in (a) with downward magnetization, and half these pillars flipped upward in (c) are presented in yellow circles, suggesting a "liberation" in magnetization during illumination. (d−f) Schematic illustration of the process of magnetic domain flipping during the illumination by ultrafast Ti:sapphire laser pulses. (d) Application of a large out-of-plane magnetic field (7 T) to magnetize all nanopillars downward. (e) Introduction of light on the nanostructured thin film to expand the lattice of SRO and release the vertical compressive strain of CFO. (f) Removal of light, resulting in the magnetization of the CFO nanopillars becoming either upward or downward for the energetically preferred state.

mostly magnetized downward by the external magnetic field, while a small portion of the scanned area relaxes to upward magnetization to minimize the local magnetostatic energy. After illuminating the sample, it is found that the coverage of the bright area reduces to ~50.5% of the total area of the MFM image, showing that half of the CFO nanopillars are magnetized downward and the other half are magnetized upward. A scenario shown in Figure 5d−f is proposed here to explain the change of the magnetization with laser illumination: initially CFO nanopillars are magnetized downward in a 7T OOP field (Figure 5d); during the laser illumination the SRO matrix extends its *c*-axis because of the photostriction effect; the elongated SRO *c*-axis then (partially) relaxes the OOP compressive strain in the CFO nanopillars and effectively reduces their magnetic anisotropy (evidenced by the MOKE measurement); the reduction of magnetic anisotropy resets, or liberates, the preferred magnetization direction of the CFO pillars (Figure 5e); after the illumination is removed and the magnetic anisotropy is restored, some of the "liberated" pillars redirect their magnetization opposite the initial direction, yielding an increase in the number of CFO pillars with upward magnetization as well as a reduction of the bright contrast in the MFM measurement (Figure 5f).

CONCLUSION

In summary, we have synthesized oxide nanostructures with CFO nanopillars embedded in a SRO matrix. Heteroepitaxy has been observed in the CFO nanopillars with an IP tensile strain and an OOP compressive strain. Ferromagnetism of CFO is found to be retained in the form of a pillar with an anisotropic easy axis toward the OOP direction due to the biaxial epitaxial strain from the SRO matrix. Photostriction of the SRO matrix has been observed. A combination of these properties in the intimately assembled CFO−SRO nanostructures leads to a light-induced, ultrafast change in magnetization of the CFO nanopillars. Our experiments on the CFO−SRO nanostructures have successfully introduced light as a potential external control to manipulate the magnetic properties in oxides. Our work demonstrates a novel concept on oxide nanostructure design and opens an alternative pathway to the traditional routes for the explorations of diverse functionalities in heteroepitaxial self-assembled oxide nanostructures.

Methods. *Sample Fabrication.* A dual-target system of bulk $SrRuO_3$ (SRO) and bulk $CoFe_2O_4$ (CFO) discs mounted on a computer-controlled exchanging stage was used to fabricate epitaxial CFO−SRO self-assembled nanostructures on a (001)-oriented $SrTiO_3$

(STO) substrate by pulsed laser deposition (PLD) with a KrF (λ = 248 nm) excimer laser. A high-pressure reflection high-energy electron diffraction (RHEED) system was positioned *in situ* to monitor the surface diffraction during the deposition to ensure the growth conditions in each alternation cycle. Samples were deposited at the substrate temperature of 750 °C and in a dynamic oxygen pressure of 100 mTorr. The deposition rates of CFO (12 Å/min) and SRO (26 Å/min) were confirmed by measuring a single layer *via* X-ray reflectivity and scanning electron microscopy measurements (not shown). Thereby, we operated of 75 and 60 shots/cycle with a repetition rate of 10 Hz for the CFO and SRO growth, respectively, in order to modulate the ratio of CFO to SRO around 0.35−0.4, and the total number of alternation cycles was set at 250 periods. After the thin-film growth, samples were cooled to room temperature at an oxygen pressure of around 1 atm.

Characterization of Structure and Physical Properties. High-resolution symmetry and asymmetry X-ray diffraction techniques were used to verify the epitaxial relationship between SRO, CFO, and STO structures in beamline BL13B and BL17B at the National Synchrotron Radiation Research Center (NSRRC), Taiwan. The interface microstructure was further studied by cross-section transmission electron microscopy. Surface morphology (AFM) and magnetic domains (MFM) studies in lift mode and conducting SRO matrix (CAFM) in contact mode were performed using a Bruker Multimode VIII. The magnetism of the CFO−SRO nanostructures was studied using SQUID magnetometry measurements, and it was checked with X-ray magnetic circular dichroism in Beamline 4.02 at Advanced Light Source, Lawrence Berkeley National Laboratory. Before studying the coupling between the SRO matrix and CFO nanopillars, samples were initially magnetized at 7 T in SQUID. Samples were then exposed to a Ti:sapphire laser operated at a repetition rate of 5.2 MHz in a pump−probe measurement. The wavelengths of the pump beam and the probe beam were set at 400 and 800 nm, respectively, to examine the photostriction effect in the SRO matrix. The MOKE measurements for probing the optical-modulation magnetic moment in the CFO/SRO samples were performed by using a HeNe laser (λ = 632.8 nm) as a probe beam and a regenerative amplifier (repetition rate of 5 kHz and wavelength of 800 nm) as a pump beam. The incident angles of the pump and probe beams were 5° and 30°, respectively. The polarizations of both pump and probe beams were parallel to the incident plane. Finally, the variation of magnetic domains was evidenced by MFM measurements.

Conflict of Interest: The authors declare no competing financial interest.

Acknowledgment. The work at National Chiao Tung University is supported by the National Science Council, R.O.C., under contract No. NSC 100-2119-M-009-003 and NSC 98-2112-M-009-008-MY3. The work at National Cheng Kung University is supported by the National Science Council, R.O.C., under contract No. NSC 99-2112-M-006-012-MY3.

REFERENCES AND NOTES

1. Takagi, H.; Hwang, H. Y. An Emergent Change of Phase for Electronics. *Science* **2010**, *327*, 1601–1602.
2. Mannhart, J.; Schlom, D. G. Oxide Interfaces—An Opportunity for Electronics. *Science* **2010**, *327*, 1607–1611.
3. Schlom, D. G.; Chen, L. Q.; Pan, X. Q.; Schmehl, A.; Zurbuchen, M. A. A Thin Film Approach to Engineering Functionality into Oxides. *J. Am. Ceram. Soc.* **2008**, *91*, 2429–2454.
4. Martin, L. W.; Chu, Y. H.; Ramesh, R. Advances in the Growth and Characterization of Magnetic, Ferroelectric, and Multiferroic Oxide Thin Films. *Mater. Sci. Eng. R* **2010**, *68*, 89–133.
5. MacManus-Driscoll, J. L. Self-Assembled Heteroepitaxial Oxide Nanocomposite Thin Film Structures: Designing Interface-Induced Functionality in Electronic Materials. *Adv. Funct. Mater.* **2010**, *20*, 2035–2045.
6. Nan, C. W.; Bichurin, M. I.; Dong, S. X.; Viehland, D.; Srinivasan, G. Multiferroic Magnetoelectric Composites: Historical Perspective, Status, and Future Directions. *J. Appl. Phys.* **2008**, *103*, 031101.
7. Moshnyaga, V.; Damaschke, B.; Shapoval, O.; Belenchuk, A.; Faupel, J.; Lebedev, O. I.; Verbeeck, J.; van Tendeloo, G.; Mücksch, M.; Tsurkan, V.; *et al*. Structural Phase Transition at the Percolation Threshold in Epitaxial $(La_{0.7}Ca_{0.3}MnO_3)_{1-x}$:$(MgO)_x$ Nanocomposite Films. *Nat. Mater.* **2003**, *2*, 247–252.
8. Zheng, H.; Wang, J.; Lofland, S. E.; Ma, Z.; Mohaddes-Ardabili, L.; Zhao, T.; Salamanca-Riba, L.; Shinde, S. R.; Ogale, S. B.; Bai, F.; *et al*. Multiferroic $BaTiO_3$-$CoFe_2O_4$ Nanostructures. *Science* **2004**, *303*, 661–663.
9. Zheng, H.; Straub, F.; Zhan, Q.; Yang, P. L.; Hsieh, W. K.; Zavaliche, F.; Chu, Y. H.; Dahmen, U.; Ramesh, R. Self-Assembled Growth of $BiFeO_3$—$CoFe_2O_4$ Nanostructures. *Adv. Mater.* **2006**, *18*, 2747–2752.
10. Levin, I.; Li, J. H.; Slutsker, J.; Roytburd, A. L. Design of Self-Assembled Multiferroic Nanostructures in Epitaxial Films. *Adv. Mater.* **2006**, *18*, 2044–2047.
11. Dix, N.; Muralidharan, R.; Rebled, J.-M.; Estrsdé, S.; Peiró, F.; Varela, M.; Fontcuberta, J.; Sánchez, F. Selectable Spontaneous Polarization Direction and Magnetic Anisotropy in $BiFeO_3$—$CoFe_2O_4$ Epitaxial Nanostructures. *ACS Nano* **2010**, *4*, 4955–4961.
12. Liao, S. C.; Tsai, P. Y.; Liang, C. W.; Liu, H. J.; Yang, J. C.; Lin, S. J.; Lai, C. H.; Chu, Y. H. Misorientation Control and Functionality Design of Nanopillars in Self-Assembled Perovskite—Spinel Heteroepitaxial Nanostructures. *ACS Nano* **2011**, *5*, 4118–4122.
13. Zavaliche, F.; Zheng, H.; Mohaddes-Ardabili, L.; Yang, S. Y.; Zhan, Q.; Shafer, P.; Reilly, E.; Chopdekar, R.; Jia, Y.; Wright, P.; *et al*. Electric Field-Induced Magnetization Switching in Epitaxial Columnar Nanostructures. *Nano Lett.* **2005**, *5*, 1793–1796.
14. Zavaliche, F.; Zhao, T.; Zheng, H.; Straub, F.; Cruz, M. P.; Yang, P. L.; Hao, D.; Ramesh, R. Electrically Assisted Magnetic Recording in Multiferroic Nanostructures. *Nano Lett.* **2007**, *7*, 1586–1590.
15. Chen., A. P.; Bi, Z. X.; Tsai, C. F.; Lee, J. H.; Su, Q.; Zhang, X. H.; Jia, Q. X.; MacManus-Driscoll, J. L.; Wang, H. Y. Tunable Low-Field Magnetoresistance in $(La_{0.7}Sr_{0.3}MnO_3)_{0.5}$:$(ZnO)_{0.5}$ Self-Assembled Vertically Aligned Nanocomposite Thin Films. *Adv. Funct. Mater.* **2011**, *21*, 2423–2429.
16. Yang, H.; Wang, H. Y.; Yoon, J.; Wang, Y. Q.; Jain, M.; Feldmann, D. M.; Dowden, P. C.; MacManus-Driscoll, J. L.; Jia, Q. X. Vertical Interface Effect on the Physical Properties of Self-Assembled Nanocomposite Epitaxial Films. *Adv. Mater.* **2009**, *21*, 3794–3798.
17. Harrington, S. A.; Zhai, J.; Denev, S.; Gopalan, V.; Wang, H.; Bi, Z. X.; Redfern, S. A. T.; Baek, S.-H.; Bark, C. W.; Eom, C.-B.; *et al*.

Thick Lead-Free Ferroelectric Films with High Curie Temperatures through Nanocomposite-Induced Strain. *Nat. Nanotechnol.* **2011**, *6*, 491–195.
18. Korff Schmising, C. v.; Harpoeth, A.; Zhavoronkov, N.; Ansari, Z.; Aku-Leh, C.; Woerner, M.; Elsaesser, T.; Bargheer, M.; Schmidbauer, M.; Vrejoiu, I.; *et al*. Ultrafast Magnetostriction and Phonon-Mediated Stress in a Photoexcited Ferromagnet. *Phys. Rev. B* **2008**, *78*, 060404(R).
19. Korff Schmising, C. v.; Bargheer, M.; Kiel, M.; Zhavoronkov, N.; Woerner, M.; Elsaesser, T.; Vrejoiu, I.; Hesse, D.; Alexe, M. Coupled Ultrafast Lattice and Polarization Dynamics in Ferroelectric Nanolayers. *Phys. Rev. Lett.* **2007**, *98*, 257601.
20. Khizroev, S.; Litvinov, D. *Perpendicular Magnetic Recording*; Springer: New York, 2005; pp 127−161.
21. Tsunashima, S. Magneto-Optical Recording. *J. Phys. D: Appl. Phys.* **2001**, *34*, R87–R102.
22. Belotelov, V. I.; Kotov, V. A.; Zvezdin, A. K. New Magneto-Optical Materials on a Nanoscale. *Phase Transitions* **2006**, *79*, 1135–1171.
23. Yang, C. H.; Yildiz, F.; Lee, S. H.; Jeong, Y. H.; Chon, U.; Koo, T. Y. Synthesis of Nanoscale Composites of Exchange Biased $MnFe_2O_4$ and Mn-Doped $BiFeO_3$. *Appl. Phys. Lett.* **2007**, *90*, 163116.
24. Zhan, Q.; Yu, R.; Crane, S. P.; Zheng, H.; Kisielowski, C.; Ramesh, R. Structure and Interface Chemistry of Perovskite-Spinel Nanocomposite Thin Films. *Appl. Phys. Lett.* **2006**, *89*, 172902.
25. Bozorth, R. M.; Tilden, E. F.; Williams, A. J. Anisotropy and Magnetostriction of Some Ferrites. *Phys. Rev.* **1955**, *99*, 1788–1799.
26. Thomsen, C.; Grahn, H. T.; Maris, H. J.; Tauc, J. Surface Generation and Detection of Phonons by Picosecond Light Pulses. *Phys Rev. B* **1986**, *34*, 4129–4138.